

Ring Polymer Molecular Dynamics with Electronic Transitions

Ruji Zhao,^{1,2} Peiwei You^{1,2} , and Sheng Meng^{1,2,3,*}

¹*Beijing National Laboratory for Condensed Matter Physics and Institute of Physics, Chinese Academy of Sciences, Beijing 100190, China*

²*School of Physical Sciences, University of Chinese Academy of Sciences, Beijing 100049, China*

³*Songshan Lake Materials Laboratory, Dongguan, Guangdong 523808, China*

 (Received 8 March 2022; revised 25 May 2022; accepted 20 March 2023; published 19 April 2023)

Full quantum dynamics of molecules and materials is of fundamental importance, which requires a faithful description of simultaneous quantum motions of the electron and nuclei. A new scheme is developed for nonadiabatic simulations of coupled electron-nuclear quantum dynamics with electronic transitions based on the Ehrenfest theorem and ring polymer molecular dynamics. Built upon the isomorphic ring polymer Hamiltonian, time-dependent multistate electronic Schrödinger equations are solved self-consistently with approximate equation of motions for nuclei. Each bead bears a distinct electronic configuration and thus moves on a specific effective potential. This independent-bead approach provides an accurate description of the real-time electronic population and quantum nuclear trajectory, maintaining a good agreement with the exact quantum solution. Implementation of first-principles calculations enables us to simulate photoinduced proton transfer in $\text{H}_2\text{O}-\text{H}_2\text{O}^+$ where we find a good agreement with experiment.

DOI: [10.1103/PhysRevLett.130.166401](https://doi.org/10.1103/PhysRevLett.130.166401)

Full quantum dynamics of molecules and materials is of fundamental importance, but it remains one of the major challenges for contemporary science. It requires an accurate description of simultaneous quantum dynamics of electrons and nuclei, which are nevertheless computationally prohibitive for realistic materials. Existing methods including the multiconfiguration time-dependent Hartree method [1,2], the variational multiconfigurational Gaussian method [3], and exact factorization [4] shed light on our fundamental understanding of correlated electron-nuclear states. They also serve as benchmark calculations for model systems but are not yet readily applicable for simulations of real materials. To date, most dynamical calculations in materials science and quantum chemistry have invoked classical nuclei approximation within a mixed quantum-classical framework such as surface hopping [5] and Ehrenfest dynamics [6], which are widely adopted to simulate photoinduced phase transitions [7,8], photocatalysis [9,10], and carrier dynamics [11,12].

However, in many domains, nuclear quantum effects (NQEs) are of fundamental importance especially for systems containing light elements, at low temperatures, or under strong photoexcitations. Examples include hydrogen bonds in water [13], quantum paraelectric materials [14,15], atom-tunneling-assisted phonon scattering [16], and even the evolution of life [17]. To consider NQEs, ring polymer molecular dynamics (RPMD) [18] becomes the mainstream choice, where a set of replicas (beads) of the system under consideration are coupled together by harmonic interactions to simulate the effect of a nuclear wave packet based on Feynman's path integral approach [19]. Regular RPMD is

constrained to adiabatic simulations of ground state properties. However, with the rise of ultrafast lasers and surging new phenomena in ultrafast science, a new demand for a quantum description of simultaneous electronic and nuclear dynamics emerges. For instance, Yang *et al.* [20] observed a transient hydrogen bond contraction by 0.04 Å in liquid water within 80 fs upon ultrafast laser excitation, which can be successfully explained only if the quantum Wigner distributions of O and H atoms are considered. Light-induced ferroelectricity in a quantum-paraelectric material SrTiO_3 also requires a description of the simultaneous quantum movement of ions and photoexcited electrons [21,22]. These works exemplify the urgent need to develop new simulation tools to tackle full quantum motions of coupled electrons and nuclei in a systematic and standardized way, while preserving the accuracy of state-of-the-art first-principles calculations. Such an approach, despite its paramount importance and urgency, is yet lacking.

Many efforts have been devoted to extend standard RPMD to nonadiabatic simulations, e.g., RPMD with surface hopping [23], coherent state mapping RPMD [24], and ring polymer surface hopping in isomorphic Hamiltonian [25]. The implementation of these methods in first-principles calculations is however not suitable. The outstanding challenge is to incorporate nonadiabatic effects in path-integral-based dynamic simulations, requiring efficient means to evaluate the effective potential for the ring polymer systems involving multiple electronic levels.

In this Letter, we propose a new scheme for realistic full quantum dynamic simulations exploiting the Ehrenfest

theorem along with RPMD, to incorporate both the nonadiabatic effects and NQEs in molecular dynamics simulations. The new scheme is validated by comparing the results with exact quantum solutions of a time-dependent Schrödinger equation for model Hamiltonians. Furthermore, the new scheme can be easily implemented in first-principles approaches. Adopting the real-time time-dependent density functional theory (RT-TDDFT) to treat the electronic evolutions and involving RPMD for the nuclear dynamics, we perform simulations of the photo-induced ultrafast proton transfer in water radiolysis. The lifetime of water cation is calculated to be ~ 47 fs, in good agreement with experiment.

The new scheme dubbed the independent-bead (IB) approach assumes that each bead in RPMD evolves on an independent effective potential energy surface. To demonstrate the basic idea of the IB scheme, we begin with deriving the ring polymer isomorphic Hamiltonian when multiple electronic states are involved. Consider a one-dimensional system with the Hamiltonian

$$\hat{H}(r, R) = \hat{T}_N + \hat{H}_{\text{el}}(r, R), \quad (1)$$

where \hat{T}_N is the nuclear kinetic Hamiltonian, and \hat{H}_{el} is the electronic Hamiltonian. To describe the quantum behaviors of a complex electron-nuclear system, the ring polymer Hamiltonian can be approximated starting from the quantum canonical partition function

$$Z = \text{Tr}[e^{-\beta\hat{H}}], \quad (2)$$

and the corresponding Kubo-transformed real-time correlation function [26] of operators \hat{A} and \hat{B} becomes

$$\begin{aligned} \tilde{C}_{AB}(t) = & \frac{1}{\beta Z} \int_0^\beta d\lambda \text{Tr}[e^{-(\beta-\lambda)\hat{H}} \hat{A} e^{-\lambda\hat{H}} \\ & \times e^{i\hat{H}t/\hbar} \hat{B} e^{-i\hat{H}t/\hbar}], \end{aligned} \quad (3)$$

where β is the inverse temperature $1/k_B T$, and k_B is the Boltzmann constant.

The correlation function given in Eq. (3) is difficult to calculate in most cases. A promising strategy is to map the quantum system to a classical ring polymer isomorphism with n beads according to RPMD theory, and the correlation function (assuming \hat{A} and \hat{B} are position-dependent operators) becomes [18]

$$\begin{aligned} \tilde{C}_{AB}(t) \simeq & \frac{1}{(2\pi\hbar)^n Z_n} \int d\mathbf{p}_0 \int d\mathbf{R}_0 e^{-\beta_n H_n(\mathbf{p}_0, \mathbf{R}_0)} \\ & \times A_n(\mathbf{R}_0) B_n(\mathbf{R}_t), \end{aligned} \quad (4)$$

where $\beta_n \equiv \beta/n$, $A_n(\mathbf{R}_0)$, and $B_n(\mathbf{R}_t)$ are averaging over the beads at time 0 and t . Z_n is the partition function for the classical ring polymer system

$$Z_n = \frac{1}{(2\pi\hbar)^n} \int d\mathbf{p} \int d\mathbf{R} e^{-\beta_n H_n(\mathbf{p}, \mathbf{R})}, \quad (5)$$

and H_n is the corresponding isomorphic Hamiltonian

$$H_n(\mathbf{p}, \mathbf{R}) = \sum_{k=1}^n \left[\frac{p_k^2}{2m} + \frac{m}{2\beta_n^2 \hbar^2} (R_k - R_{k-1})^2 \right] + \underline{V}(\mathbf{R}), \quad (6)$$

with a cyclic boundary condition $R_0 \equiv R_n$, and $\underline{V}(\mathbf{R}) \equiv -(1/\beta_n) \ln \sum_s \langle s | \prod_{k=1}^n e^{-\beta_n \hat{H}_{\text{el}}(R_k)} | s \rangle$ [25], where s is running over all electronic states.

The theory outlined above applies only to the equilibrium state. To make the nonadiabatic isomorphic Hamiltonian feasible for first-principles calculations, we suggest the independent-bead approximation: Each bead bears an independent electronic configuration and evolves on the mean field according to their respective electronic wave function $\Phi_{\text{el}}(r, R_k, t)$. Therefore, the effective potential can be approximated as

$$\underline{V}(\mathbf{R}) \simeq \sum_{k=1}^n V_{\text{eff}}(R_k) = \sum_{k=1}^n \langle \Phi_{\text{el}}(r, R_k, t) | \hat{H}_{\text{el}} | \Phi_{\text{el}}(r, R_k, t) \rangle. \quad (7)$$

We take the sum of mean-field V_{eff} to replace the potential $\underline{V}(\mathbf{R})$, and then the corresponding ring polymer Hamiltonian becomes

$$H_n^{\text{IB}}(\mathbf{p}, \mathbf{R}) = \sum_{k=1}^n \left[\frac{p_k^2}{2m} + \frac{m}{2\beta_n^2 \hbar^2} (R_k - R_{k-1})^2 + V_{\text{eff}}(R_k) \right]. \quad (8)$$

The approximate real-time dynamics in the nonadiabatic ring polymer system can be obtained from the trajectories of each bead associated with the isomorphic Hamiltonian, following the equations of motion [27,28]:

$$\dot{p}_k = -\frac{m}{\beta_n^2 \hbar^2} (2R_k - R_{k+1} - R_{k-1}) - \frac{\partial V_{\text{eff}}(R_k)}{\partial R_k}, \quad (9)$$

$$\dot{R}_k = \frac{p_k}{m} \quad (10)$$

for $k = 1, \dots, n$. The generalization to two or three dimensions is straightforward.

In the framework of the Ehrenfest theorem, the electronic wave function of each bead can be expanded in the adiabatic representation

$$\Phi(r, R_k, t) = \sum_{i=1} c_{i,k}(t) \varphi_i(r, R_k), \quad (11)$$

where $c_{i,k}(t)$ is the time-dependent complex coefficient. Inserting Eq. (11) into the time-dependent electronic Schrödinger equation, we have

$$i\hbar\dot{c}_{i,k} = E_i(R_k)c_{i,k} - i\hbar\sum_{j\neq i}\dot{R}_k \cdot d_{ij}(R_k)c_{j,k}, \quad (12)$$

where $d_{ij}(R)$ is the nonadiabatic coupling vector (NAC) which is responsible for the electronic transitions between different adiabatic states: $d_{ij}(R) = \langle \varphi_i(r, R) | \nabla_R | \varphi_j(r, R) \rangle_r$. The bracket $\langle \langle \rangle \rangle_r$ indicates the integral over electronic degrees of freedom only.

We then compare the IB approximation with earlier algorithms proposed by Tully and co-workers, namely, the centroid approximation (CA) and bead approximation (BA) [23]. In the CA, the centroid of a ring polymer is equivalent to the classical-like nucleus, and the evolution of electronic states depends on the centroid trajectory of ring polymer instead of the classical nuclear trajectory. Under this assumption, Eq. (12) becomes

$$i\hbar\dot{c}_i = E_i(\bar{R})c_i - i\hbar\sum_{j\neq i}\dot{\bar{R}} \cdot d_{ij}(\bar{R})c_j, \quad (13)$$

where \bar{R} and $\dot{\bar{R}}$ stand for the position and velocity of the centroid, respectively.

In the BA, the ring polymer is regarded as an effective molecule with the beads being its constituent atoms. The adiabatic PES and nonadiabatic coupling are chosen to be the PES and NAC averaged over these beads. Therefore, Eq. (12) can be expressed as

$$i\hbar\dot{c}_i = \left[\frac{1}{n} \sum_{k=1}^n E_i(R_k) \right] c_i - i\hbar \sum_{j\neq i} \left[\frac{1}{n} \sum_{k=1}^n \dot{R}_k \cdot d_{ij}(R_k) \right] c_j. \quad (14)$$

Both CA and BA assume the beads of the ring polymer necklace share the same electronic configuration, which is different from the idea of IB approximation. The schematic illustration of these three approaches is presented in Fig. 1. To evaluate the accuracy of the IB method, we apply it to several one-dimensional, two-state model problems that mimic nonadiabatic chemical reactions. Exact quantum mechanical (QM) dynamics is also performed, as well as the results obtained from the CA and BA schemes for comparison. The mass of the quantum particle is chosen to

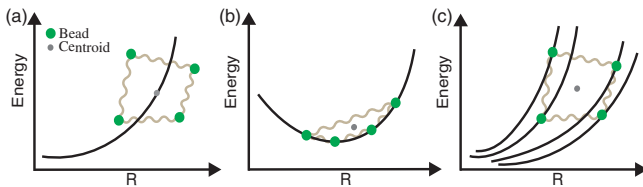


FIG. 1. Schematic diagrams for (a) centroid approximation, (b) bead approximation, and (c) independent-bead approximation approaches. The solid black lines represent the effective potential curves. Adjacent beads are connected by spring interaction (wave lines).

be the mass of a hydrogen atom. To avoid redundancy, we mainly focus on the results obtained for the simple avoided crossing model and the others are shown in Supplemental Material [29].

In the diabatic representation, the potential of a simple avoided crossing model is expressed as $V_{11} = A(1 - e^{-BR})$ for $R \geq 0$; $V_{11} = -A(1 - e^{BR})$ for $R < 0$; $V_{22} = -V_{11}$; $V_{12} = V_{21} = Ce^{-DR^2}$, where V_{11} and V_{22} are diabatic potential energy surfaces, and V_{12} is the off-diagonal coupling matrix element between the two. The parameters used for calculations are chosen to be $A = 0.27$ eV, $B = 7.56 \text{ \AA}^{-1}$, $C = 1.36 \times 10^{-1}$ eV, $D = 22.33 \text{ \AA}^{-2}$. The two adiabatic potentials and NAC strength are shown in Fig. 2(a).

The system is initially prepared in the ground state, and the nucleus is located at $R_0 = -1.59 \text{ \AA}$ with initial velocity $v_0 = 0.13 \text{ \AA/fs}$. In total, 200 beads are used in the RPMD calculations at 50 K, and the FWHM of the initial wave packet is identical to that of the ‘‘ring polymer’’ packet. Note that in the RPMD-IB scheme, the electronic population is averaged over all beads.

Figure 2(b) shows the time evolution of the electronic population in the excited state using different methods. The real-time electronic transition obtained by the conventional Ehrenfest dynamics shows a rapid increase due to the missing NQE. The RPMD-CA shows agreement with the Ehrenfest results for the evolution equations in Eq. (13) only using the centroid trajectory. As for the results of RPMD-BA scheme, it is completely inconsistent with the exact quantum mechanical results, due to the inaccurate effective potential induced in Eq. (14). On the other hand, the IB approach shows an excellent agreement with the exact QM results, whether the nucleus is in the strong NAC region or leaves it.

Most importantly, we divide these beads into the two states according to their population, and then compare the normalized histograms of their respective spatial distribution with the profile from the exact solution at different time. As shown in Fig. 3, during the tunneling process, the

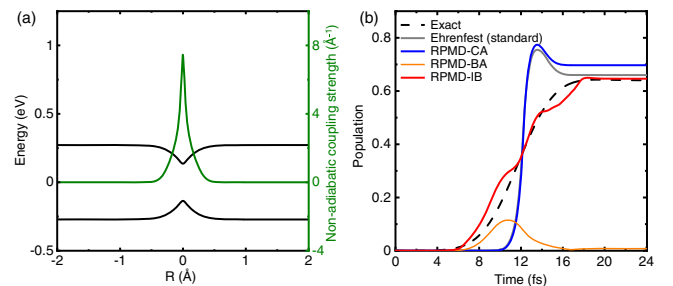


FIG. 2. (a) Two adiabatic potential energy curves (black lines) and the nonadiabatic coupling strength (green line) as a function of position R for the avoided crossing model. (b) The real-time electronic population in the excited state obtained by different methods.

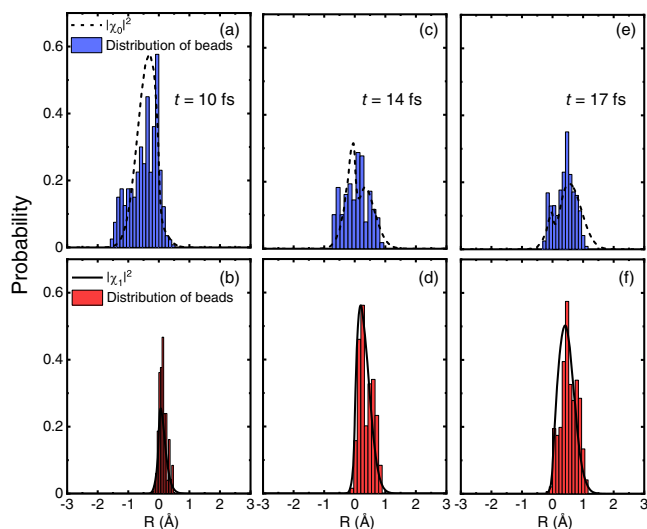


FIG. 3. Comparisons between spatial distribution of beads from RPMD-IB simulation and the wave packet profile from exact solution. All beads are divided into two states according to their electronic occupation. The wave packet is plotted as $|\chi_i|^2$ ($i = 0, 1$), where 0 and 1 refer to the ground and excited states, respectively. The blue bar denotes the beads population in ground state in (a), (c), and (e), and the beads population in the excited state is represented by the red bar in (b), (d), and (f). We compared these two kinds of distributions at $t = 10$ fs [(a) and (b)], $t = 14$ fs [(c) and (d)], and $t = 17$ fs [(e) and (f)], respectively.

histogram of the bead distribution and the QM wave packet show a good agreement, indicating that the quantized nucleus is successfully mapped onto the ring polymer in the IB approach.

We have shown that the IB approximation of the isomorphic Hamiltonian in Eq. (6) is reasonable according to its performance in several model systems [29]. Moreover, the IB scheme can be applied but not limited to these empirical model calculations. To validate the IB scheme for simulations of real materials, we develop it in the first-principles code TDAP which goes beyond the former *ad hoc* algorithm [28]. The TDDFT works with our RPMD-IB approach in the following way: We solve the RT-TDDFT equation for each bead $i\hbar(\partial/\partial t)\Phi_j(\mathbf{r}, \mathbf{R}, t) = \hat{H}_{\text{eff}}^j(\mathbf{r}, \mathbf{R}, t)\Phi_j(\mathbf{r}, \mathbf{R}, t)$. Here, $\hat{H}_{\text{eff}}^j(\mathbf{r}, \mathbf{R}, t) = \hat{H}_{\text{BO}}^j(\mathbf{r}, \mathbf{R}) + U_{\text{ext}}(\mathbf{r}, \mathbf{R}, t)$, where $\hat{H}_{\text{BO}}^j(\mathbf{r}, \mathbf{R})$ is the traditional Born-Oppenheimer Hamiltonian for each bead, and $U_{\text{ext}}(\mathbf{r}, \mathbf{R}, t)$ is the external field. For RPMD simulations, the potential in the nuclear Hamiltonian and forces are evaluated by TDDFT.

Here we take the real-time nonadiabatic dynamics of water radiolysis in $\text{H}_2\text{O}-\text{H}_2\text{O}^+$ as an example. Although the RPMD-IB requires a large number of beads and induces heavier computational cost, the time consumed is only a few times more than the traditional TDDFT calculation thanks to the parallel strategy. Moreover, when the system is large, the IB scheme can be applied to a certain group of atoms, while the other atoms are treated as classical particles, and therefore, the computational complexity can be further

reduced [29]. Experiments show that the H_2O^+ cation is extremely unstable in liquid and undergoes proton transfer to an adjacent water molecule in 46 ± 10 fs [20,32–34].

The gamma k grid and Perdew-Burke-Ernzerhof functional are used in the TDDFT simulations, as well as Troullier-Martins pseudopotentials, double zeta polarization basis set, and plane-wave energy cutoff of 200 Ry for charge density [29]. To represent the initial photoexcited state, hole concentration of 1/6 is used in line with experiment and preceding surface hopping simulations [34]. There are 12 beads employed to meet the convergence of simulations. Calculation details are presented in Supplemental Material [29].

Figure 4 displays the main results of the RPMD-IB simulation. Upon photoexcitation, the hole is initially located at the second water molecule ($w2$), as shown in the right panel of Fig. 4(a). The time evolution of δ defined as the distance difference of the hydrogen atom (H) to its two neighboring oxygen atoms (O1, O2) is shown in the left panel of Fig. 4(a). For comparison, δ keeps oscillating in the Ehrenfest dynamics simulations, stemming from the neglect of NQEs, where the water molecules are always intact. When considering NQEs using the IB scheme, we find δ decreases to -0.2 Å at ~ 47 fs after photoexcitation, validating the ultrafast nature of proton transfer and the formation of a hydronium cation (H_3O^+) and hydroxyl

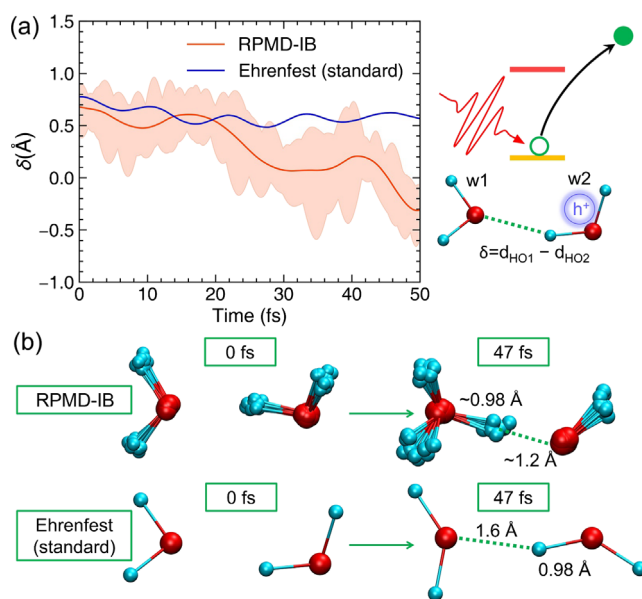


FIG. 4. (a) The distance difference of the hydrogen atom (H) and its two nearest oxygen atoms (O1, O2). Shadows indicate the quantum fluctuation of all beads. Schematic setting is shown in the right panel. (b) The snapshots at 0 and 47 fs in the excited-state dynamics. In the RPMD-IB simulation, the configurations of all beads are presented. At 47 fs, the whole nuclear wave packet of split hydrogen atom approaches the oxygen atom (O1) of the first water molecule, indicating the formation of hydronium (H_3O^+) and OH radical.

radical ($\text{OH}\cdot$). The shadows in Fig. 4(a) display the quantum fluctuation of δ estimated by overlaying the δ for all beads. Time evolution of atomic configurations using the Ehrenfest and RPMD-IB scheme is presented in Fig. 4(b). The RPMD-IB approach yields the lifetime of $47\text{--}50$ fs for H_2O^+ , which is in good agreement with the experiment ($\sim 46 \pm 10$ fs) [34], while the water molecules do not dissociate in Ehrenfest dynamics simulations.

Figure 5 shows the evolution of electronic states during the proton transfer process. We focus on the two hydrogen atoms of the second water (w_2) [labeled H1_{w_2} and H2_{w_2} in Fig. 5(b)]. The variation of electron distribution on H1_{w_2} and H2_{w_2} is presented in Fig. 5(a). In contrast to the Ehrenfest simulation, the H2_{w_2} shows a clear reduction before 20 fs using RPMD-IB. This trend can be ascribed to the quantum fluctuation of atomic configurations, which

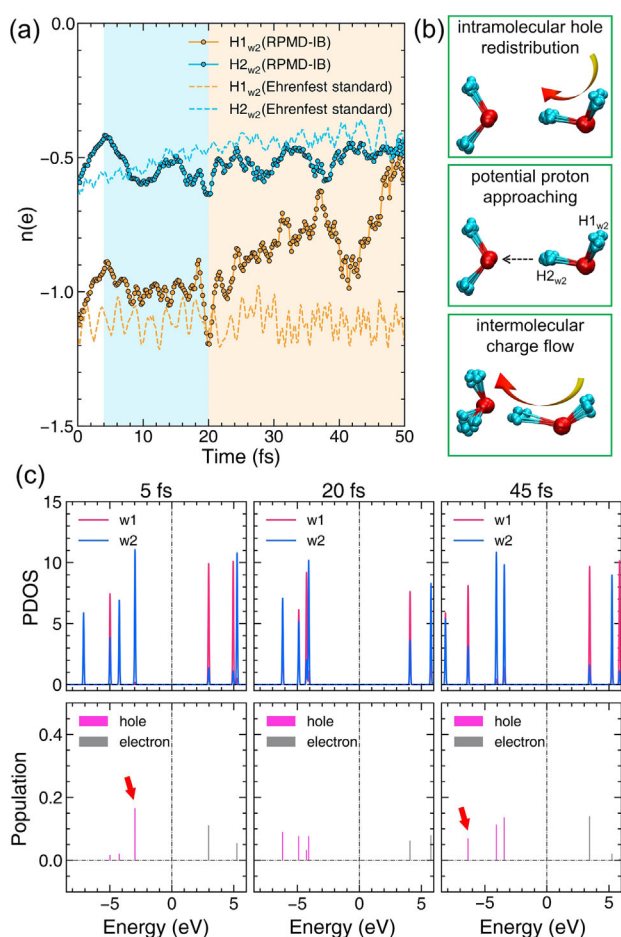


FIG. 5. (a) The time evolution of the Hirshfeld electron occupation for two hydrogen atoms in the second water molecule obtained from the Ehrenfest and RPMD-IB simulations. We averaged the Hirshfeld charges over all beads in the RPMD-IB simulation. (b) The atomic mechanism for the formation of hydronium and OH radical. (c) The projected density of states on the two water molecules (upper panel) and the population of each energy level (lower panel) at 5, 20, and 45 fs. We choose a typical bead to represent the evolution of electronic structure.

leads to intramolecular hole redistribution and enhances the Coulomb attraction between H2_{w_2} and O1 . The second trend is the increase of electrons on H1_{w_2} in the period of 20–50 fs, implying a charge flow from the second water (w_2) to the first water (w_1). This process is accompanied by the proton transfer from w_2 to w_1 . The charge-driven proton transfer mechanism is schematically displayed in Fig. 5(b). Moreover, the projected density of states (PDOS) of each water molecule is shown in Fig. 5(c). In the beginning at 5 fs, the hole population and separated PDOS distribution demonstrate the hole is mainly localized on w_2 . At 20 fs, the diffusive PDOS and hole population indicate a transforming water dimer structure, which can be regarded as the precursor state before the formation of hydronium. The accompanying intermolecular charge flow during the formation of the H_3O^+ and OH radical can also be identified in the PDOS and hole population at 45 fs, where some holes have been transported to w_1 . The corresponding electronic density of a typical bead is shown in Fig. S4 of the Supplemental Material [29].

We also simulate the proton transfer process in liquid water as shown in Fig. S5 of the Supplemental Material [29], where a similar agreement can be achieved. RPMD-CA and RPMD-BA are also implemented in our first-principles code. The results shown in Fig. S3 of the Supplemental Material [29] are at variance with experimental data. This may arise from the inconsistency between nuclear forces of the beads and electronic states [29]. Moreover, the proposed RPMD-IB scheme can deal with large and extended systems and is not limited to small clusters. We have simulated two additional processes, i.e., collision of a hydrogen atom with graphene and photocatalytic water splitting on TiO_2 , with the simulation cell containing 33 and 195 atoms, respectively. The electron transfer is accelerated compared to conventional Ehrenfest dynamics for both systems due to quantum fluctuations. In addition, the computational cost is only a few times more than original TDDFT calculations. Full details are reported in Secs. VI and VII of the Supplemental Material [29].

In conclusion, we demonstrate how the RPMD algorithm and Ehrenfest theorem can be combined in a simple effective computational scheme that accurately reproduces the exact electronic transition rate and nuclear quantum dynamics in nonadiabatic processes. Moreover, the simulated lifetime of hole in $\text{H}_2\text{O}\text{--}\text{H}_2\text{O}^+$ agrees with the experiment: Proton transfer occurs at 47 fs thanks to the quantum nature of atoms. These encouraging results indicate that the RPMD-IB approach is readily applicable to more realistic multidimensional material systems where electronic transitions and nuclear quantum effects play an indispensable role.

We acknowledge Q. Chen, D. Q. Chen, X. Z. Li, and E. G. Wang for help on codes and discussion. This work is

supported by MOST (Grant No. 2021YFA1400201), NSFC (Grants No. 12025407 and No. 11934003), and CAS (Grants No. XDB330301 and No. YSBR047).

R. Z. and P. Y. contributed equally to this work.

*smeng@iphy.ac.cn

- [1] U. Manthe, H.-D. Meyer, and L. S. Cederbaum, *J. Chem. Phys.* **97**, 3199 (1992).
- [2] H.-D. Meyer, U. Manthe, and L. Cederbaum, *Chem. Phys. Lett.* **165**, 73 (1990).
- [3] G. Richings, I. Polyak, K. Spinlove, G. Worth, I. Burghardt, and B. Lasorne, *Int. Rev. Phys. Chem.* **34**, 269 (2015).
- [4] A. Abedi, N. T. Maitra, and E. K. U. Gross, *Phys. Rev. Lett.* **105**, 123002 (2010).
- [5] J. C. Tully, *J. Chem. Phys.* **93**, 1061 (1990).
- [6] P. Ehrenfest, *Z. Phys.* **45**, 455 (1927).
- [7] M.-X. Guan, E. Wang, P.-W. You, J.-T. Sun, and S. Meng, *Nat. Commun.* **12**, 1885 (2021).
- [8] N.-K. Chen, X.-B. Li, J. Bang, X.-P. Wang, D. Han, D. West, S. Zhang, and H.-B. Sun, *Phys. Rev. Lett.* **120**, 185701 (2018).
- [9] P. You, C. Lian, D. Chen, J. Xu, C. Zhang, S. Meng, and E. Wang, *Nano Lett.* **21**, 6449 (2021).
- [10] A. V. Akimov, J. T. Muckerman, and O. V. Prezhdo, *J. Am. Chem. Soc.* **135**, 8682 (2013).
- [11] K. Ni, J. Du, J. Yang, S. Xu, X. Cong, N. Shu, K. Zhang, A. Wang, F. Wang, L. Ge, J. Zhao, Y. Qu, K. S. Novoselov, P. Tan, F. Su, and Y. Zhu, *Phys. Rev. Lett.* **126**, 027402 (2021).
- [12] X. Jiang, Q. Zheng, Z. Lan, W. A. Saidi, X. Ren, and J. Zhao, *Sci. Adv.* **7**, eabf3759 (2021).
- [13] J. Guo, J.-T. Lü, Y. Feng, J. Chen, J. Peng, Z. Lin, X. Meng, Z. Wang, X.-Z. Li, E.-G. Wang *et al.*, *Science* **352**, 321 (2016).
- [14] D. Shin, S. Latini, C. Schäfer, S. A. Sato, U. De Giovannini, H. Hübener, and A. Rubio, *Phys. Rev. B* **104**, L060103 (2021).
- [15] K. A. Müller and H. Burkard, *Phys. Rev. B* **19**, 3593 (1979).
- [16] B. Sun, S. Niu, R. P. Hermann, J. Moon, N. Shulumba, K. Page, B. Zhao, A. S. Thind, K. Mahalingam, J. Milam-Guerrero *et al.*, *Nat. Commun.* **11**, 6039 (2020).
- [17] F. Trixler, *Curr. Org. Chem.* **17**, 1758 (2013).
- [18] I. R. Craig and D. E. Manolopoulos, *J. Chem. Phys.* **121**, 3368 (2004).
- [19] R. P. Feynman, A. R. Hibbs, and D. F. Styer, *Quantum Mechanics and Path Integrals* (Courier Corporation, New York, 2010).
- [20] J. Yang, R. Dettori, J. P. F. Nunes, N. H. List, E. Biasin, M. Centurion, Z. Chen, A. A. Cordones, D. P. Deponte, T. F. Heinz *et al.*, *Nature (London)* **596**, 531 (2021).
- [21] X. Li, T. Qiu, J. Zhang, E. Baldini, J. Lu, A. M. Rappe, and K. A. Nelson, *Science* **364**, 1079 (2019).
- [22] T. F. Nova, A. S. Disa, M. Fechner, and A. Cavalleri, *Science* **364**, 1075 (2019).
- [23] P. Shushkov, R. Li, and J. C. Tully, *J. Chem. Phys.* **137**, 22A549 (2012).
- [24] S. N. Chowdhury and P. Huo, *J. Chem. Phys.* **147**, 214109 (2017).
- [25] X. Tao, P. Shushkov, and T. F. Miller, *J. Chem. Phys.* **148**, 102327 (2018).
- [26] R. Kubo, *J. Phys. Soc. Jpn.* **12**, 570 (1957).
- [27] P. You, J. Xu, C. Lian, C. Zhang, X.-Z. Li, E.-G. Wang, and S. Meng, *Electron. Struct.* **1**, 044005 (2019).
- [28] P. You, D. Chen, C. Lian, C. Zhang, and S. Meng, *WIREs Comput. Mol. Sci.* **11**, e1492 (2021).
- [29] See Supplemental Material at <http://link.aps.org/supplemental/10.1103/PhysRevLett.130.166401> for the results in other model systems, the details of first-principles simulations of hole-driven proton transfer in $\text{H}_2\text{O}-\text{H}_2\text{O}^+$, and other processes in large systems, which includes Refs. [30,31].
- [30] J. P. Perdew, K. Burke, and M. Ernzerhof, *Phys. Rev. Lett.* **77**, 3865 (1996).
- [31] T. E. Markland and D. E. Manolopoulos, *J. Chem. Phys.* **129**, 024105 (2008).
- [32] O. Marsalek, C. G. Elles, P. A. Pieniazek, E. Pluhaov, J. VandeVondele, S. E. Bradforth, and P. Jungwirth, *J. Chem. Phys.* **135**, 224510 (2011).
- [33] E. Kamarchik, O. Kostko, J. M. Bowman, M. Ahmed, and A. I. Krylov, *J. Chem. Phys.* **132**, 194311 (2010).
- [34] Z.-H. Loh, G. Doumy, C. Arnold, L. Kjellsson, S. H. Southworth, A. A. Haddad, Y. Kumagai, M.-F. Tu, P. J. Ho, A. M. March *et al.*, *Science* **367**, 179 (2020).